THREE-DIMENSIONAL NUMERICAL STUDY OF TURBULENCE IN AN ENTRAINING MIXED LAYER

J. W. DEARDORFF

National Center for Atmospheric Research, Boulder Colo. U.S.A.*

(Received 4 February, 1974)

Abstract. The mean structure calculated by a three-dimensional numerical model of a heated planetary boundary layer, in simulation of DAY 33 of the Australian Wangara data, has been previously described. The present study supplements it by describing properties of the calculated turbulence.

A major finding is the importance of entrainment upon turbulence statistics relating to specific humidity, relative to those for potential temperature. The variances, skewness and spectra of velocity, temperature and humidity are presented, as are budget equations for kinetic energy, temperature and humidity variances and heat/moisture fluxes. These are interpreted with regard to the relative importance of the surface flux vs the flux due to entrainment at the top of the mixed layer, and in regard to the structure which would occur if the entrainment were to vanish.

The Rotte-type closure assumption is tested for the correlation between the pressure fluctuation and the vertical gradient of vertical velocity, potential temperature, or specific humidity, and found to be qualitatively correct except near the top of the mixed layer.

1. Introduction

In a previous study (Deardorff, 1974, herein called D2) the mean structure within a growing, heated planetary boundary layer was studied with a three-dimensional numerical model containing $(40)^3$ grid points inside a volume of horizontal area 5 km × 5 km and height 2 km. The horizontal grid intervals were 125 m, and the vertical grid interval was 50 m. The subgrid stresses and heat/moisture fluxes were calculated from space-time dependent second-moment equations described in D2. The situation treated was DAY 33 of the Wangara data (Clarke *et al.*, 1971) between 9 a.m. and 5 p.m. with clear skies. The surface was assumed to be horizontally homogeneous in roughness and temperature. The latter was calculated from a surface energy-balance equation, a major input of which was the solar zenith angle.

In this study, the turbulence statistics from the same numerical integration will be presented. The height will be scaled by the depth, z_i, of the mixed layer (or convective clear-air boundary layer), velocities by the convective velocity scale w_* defined below, and temperature and moisture by their respective free-convection scales: θ_* and q_*. The definitions are:

$$w_* = \left(\frac{g}{\theta_v} \langle w\theta_v \rangle_s \, z_i\right)^{1/3}$$

$$\theta_* = \langle w\theta_v \rangle_s / w_*$$

$$q_* = \langle wq \rangle_s / w_* ,$$

* NCAR is sponsored by the National Science Foundation (U.S.A.).

Boundary-Layer Meteorology 7 (1974) 199–226.

where $\langle w\theta_v\rangle_s$ is the surface kinematic heat flux relative to virtual potential temperature, θ_v, and $\langle wq\rangle_s$ is the surface moisture flux relative to the specific humidity, q. The angular brackets represent the horizontal average. The vertical fluxes of momentum, heat and moisture were presented in D2, and will not be presented again here except as they enter into balance equations for the second moments.

Symbols designating different types of averaging utilized in this paper are summarized below:

u True variable
$\langle u\rangle$ Its horizontal average (over 5 km × 5 km region)
$\bar{u}$ Its local grid-volume average
u' $u-\bar{u}$
u'' $u-\langle u\rangle$
$\langle\bar{u}\rangle$ Horizontal average of $\bar{u}$
$\bar{u}''$ $\bar{u}-\langle\bar{u}\rangle$.

2. The Variances

The vertical velocity variance will be presented first. It is given by

$$\langle\overline{w^2}\rangle = \langle\bar{w}^2\rangle + \langle\overline{w'^2}\rangle \tag{1}$$

where the overbar refers to the grid-volume average and the prime to the local deviation from the local overbar average. Thus, the first term on the right of (1) is the resolvable-scale portion of the variance, and the second term is the subgrid-scale portion, the value of which depends more directly upon the subgrid closure assumptions.

In Figure 1, $\langle\overline{w^2}\rangle$ is normalized by w_*^2 and plotted vs z/z_i for four times of DAY 33. During this period, the calculated value of z_i increased from 390 to 1480 m, as shown in the Table below, and w_* nearly doubled.

TABLE

Hour	z_i (m)	z_{lid}/z_i	$-z_i/L$	w_* (cm s^{-1})	θ_* (K)	$q_* \times 10^5$	$\langle w\theta_v\rangle_s$ (cm s^{-1} K)	$\langle wq\rangle_s$ (cm s^{-1}) × 10^3
10.4	390	5.13	250	123	0.114	1.07	14.0	1.32
10.9	830	2.41	630	164	0.095	1.24	15.5	2.04
13.4	1200	1.67	1070	201	0.099	1.18	20.0	2.37
16.2	1480	1.35	350	205	0.066	1.08	13.5	2.21

Despite these large changes, the normalized variance follows a fairly unique curve, the average of which agrees well with the earlier calculations (Deardorff, 1972a, hereafter called D1) from the model having a lid at $z=z_i$. The ratio of the height of the lid in this model (D2) relative to z_i is listed in the third column of the Table. Presumably, the scatter between the four curves of Figure 1 is associated mostly with sampling

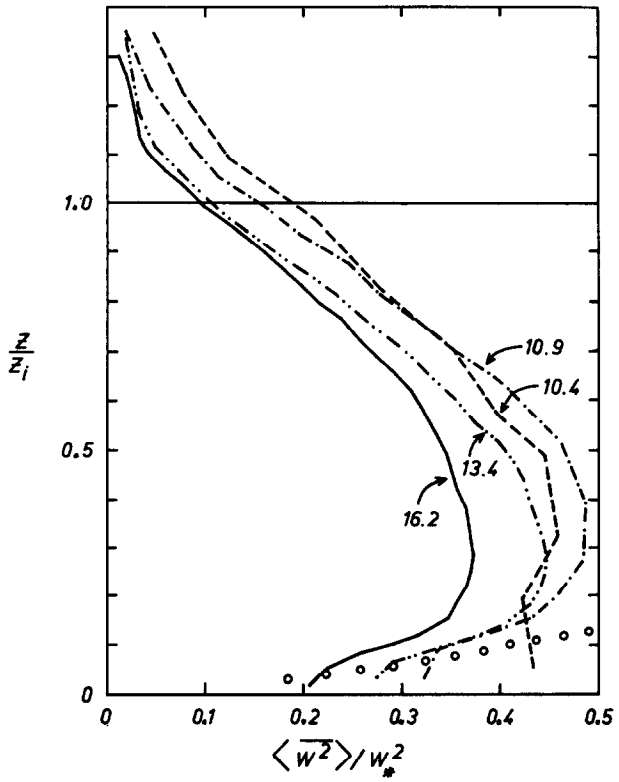

Fig. 1. Vertical profiles of dimensionless vertical velocity variance calculated for the four designated times (hour and fraction thereof) of DAY 33.

error, no averaging in time having been done here. Although this scatter is greater than expected, it is interesting to note that the curve labelled 10.4, for which only 7 grid levels lay within the mixed layer, is not particularly different from the others which had over twice as many grid levels in the mixed layer. This indicates that truncation error was not important in affecting the velocity variances.

The circles in Figure 1 represent the formula

$$\langle \overline{w^2} \rangle / w_*^2 = 1.9\,(z/z_i)^{2/3} \tag{2}$$

of Wyngaard *et al.* (1971) derived from surface-layer measurements. The formula holds to a height of roughly 0.1 z_i (except not below $z = -L$, where L is the Monin-Obukhov length).

The height, z_i, of the cloud-free boundary layer is defined here as the height at which the sensible heat flux is most negative (due to the entrainment of potentially warm air downwards). The finite value of $\langle \overline{w^2} \rangle$ at and above z_i is associated with this entrainment and also with internal waves. At $z = z_i$, $\langle \overline{w^2} \rangle$ is about 0.14 w_*^2, as compared with about 0.44 w_*^2 at the maximum which occurs in the vicinity of $z = 0.33\, z_i$.

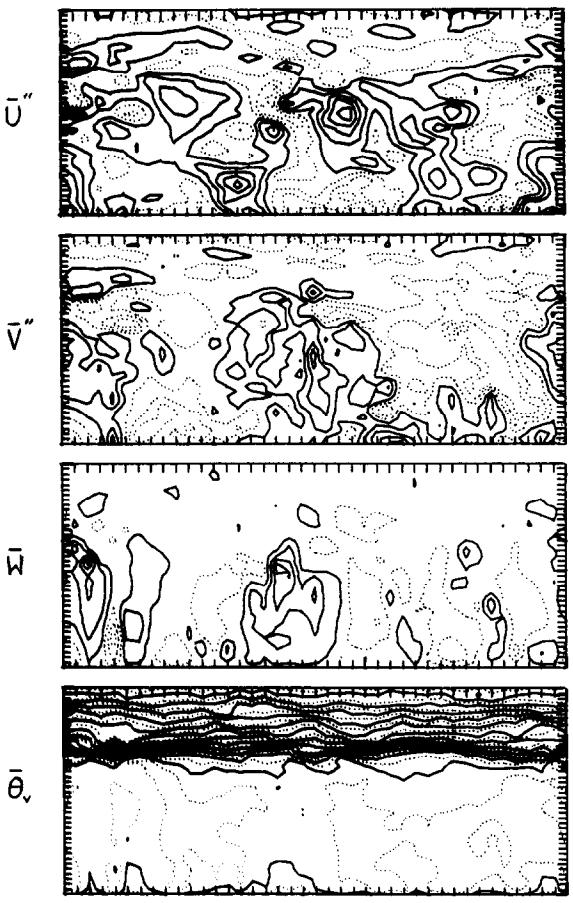

Fig. 2. Vertical cross-section (at $y = 4\ \Delta y$) of the resolvable-scale eddies at hour 14.15, for the three velocity components $\bar{u}''$, $\bar{v}''$, $\bar{w}$, and for virtual potential temperature $\bar{\theta}_v$. The mean flow has been removed from the horizontal velocity components. For $\bar{u}''$, $\bar{v}''$, $\bar{w}$, the solid contours represent values greater than the mean, the dotted contours represent values less than the mean, and the zero line lies halfway between adjacent solid and dotted contours; respective contour intervals are 0.39, 0.43, 1.10 m s^{-1}. For $\bar{\theta}_v$, the interval between solid contours is 0.5 C; contours intermediate to these are dotted. Tick marks at periphery indicate the grid intervals.

The internal waves at and above $z = z_i$ appear in the contours of $\bar{\theta}_v$ in Figure 2, which also shows the velocity components in the same $x-z$ plane. Here, x points east, the mean wind was from the southeast, but no effects of wind shear (e.g., tilted plumes) above the lowest grid interval are noticeable because the ratio $-z_i/L$ was so large, as indicated in the fourth column of the Table.

The entrainment is clearly evident in a side view of the moisture field as in Figure 3. Here it is seen how two entraining cusps of dry air are being carried downward well into the mixed layer. Sometimes the moisture contour interval and the plane of the vertical cross-section were optimal to allow such entrainment to be visible right down to the surface.

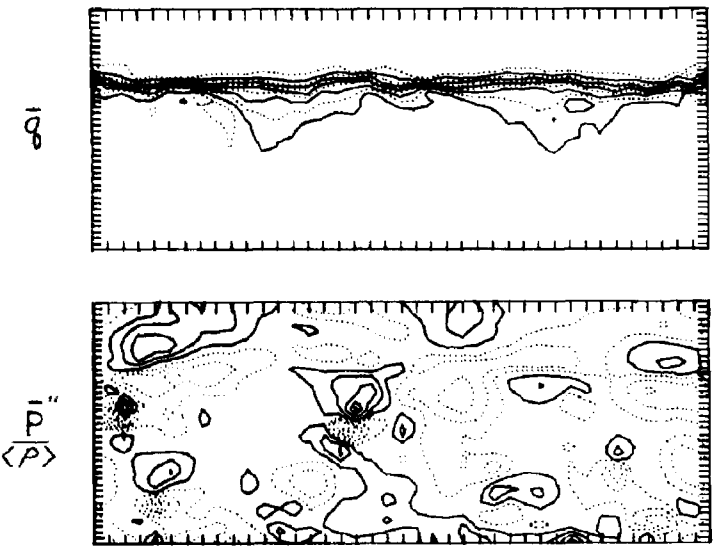

Fig. 3. Vertical ($x - z$) cross-section ($y = 4\ \Delta y$) at hour 14.15 for specific humidity, $\bar{q}$, and for pressure $\bar{p}''/\langle\rho\rangle$. The interval between solid contours of $\bar{q}$ is 0.5×10^{-3}; contours intermediate to these are dotted. For $\bar{p}''/\langle\rho\rangle$, the contour interval is 0.53 $m^2\ s^{-2}$. See also caption of Figure 2.

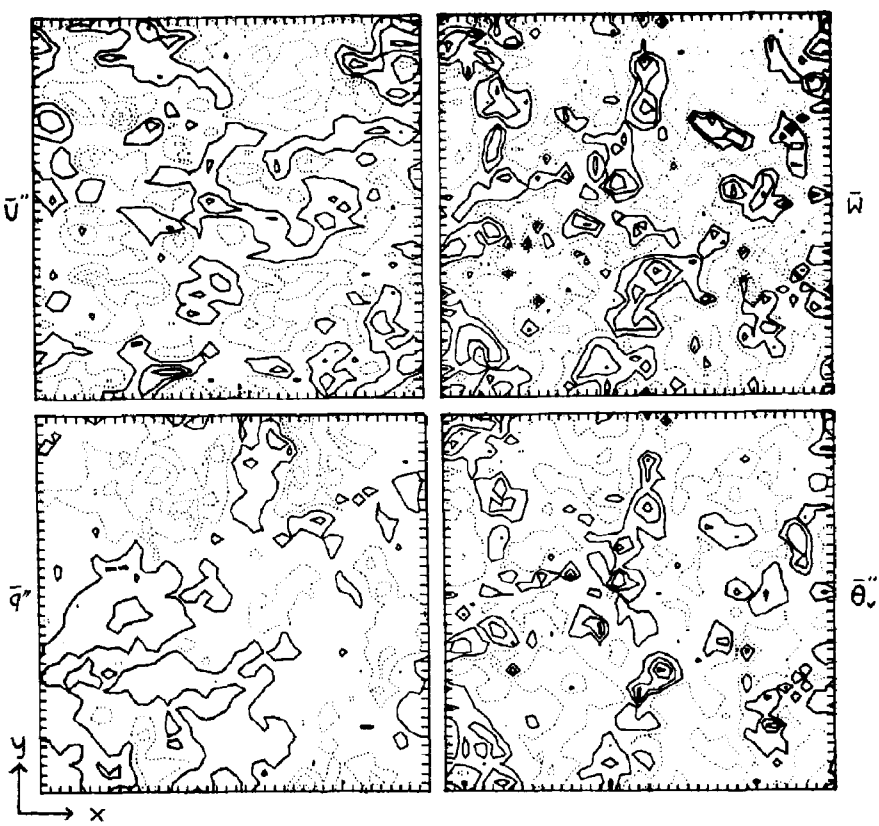

Fig. 4. Horizontal cross-section (at $z = 0.5$ km $= 0.38\ z_i$) at hour 14.15 for $\bar{u}''$, $\bar{w}$, $\bar{\theta}''_v$ and $\bar{q}''$. The contour intervals for $\bar{u}''$ and $\bar{w}$ are 0.2 and 1.1 $m\ s^{-1}$; for $\bar{\theta}''_v$ is 0.11 C; and for $\bar{q}''$ is 0.095×10^{-3}. See also the caption of Figure 2.

The vertical extent of the mixed layer shows up well in the side views of $\bar{\theta}_v$, $\bar{q}$, and $\bar{w}$. Its height is not deducible from the side view of the pressure-fluctuation field.

The fields of eddies in a horizontal plane, at the same time as in Figures 2 and 3, are shown in Figure 4. Here the random orientations of the vertical velocity and temperature eddies (clear skies, large $-z_i/L$) are rather evident. One can also see an interesting tendency for the humidity eddies of largest scale permitted by the model to be much more predominant than for the temperature eddies.

The variance of the horizontal velocity components is shown in Figure 5a for the same four times during DAY 33. The two individual components did not differ significantly, and have been averaged together. The horizontal velocity component is seen to maintain a nearly constant value in the upper half of the mixed layer, a tendency which has been recently confirmed from a laboratory study (Willis and Deardorff, 1974). The relatively rapid decrease of this variance abruptly above z_i may thus serve as an additional indicator of z_i, if observations with little sampling error are available. The magnitude of the pressure fluctuations (see Figure 5b), however, is nearly con-

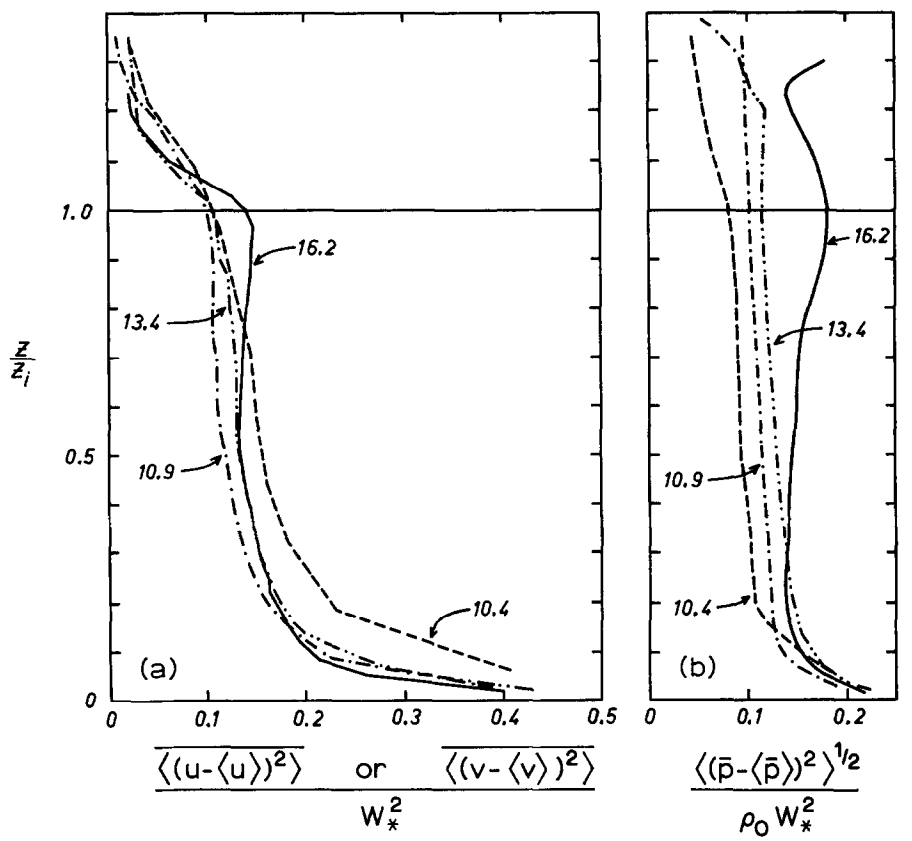

Fig. 5. Vertical profiles of dimensionless horizontal velocity variance (a), and dimensionless pressure fluctuation (b), calculated for the four designated times.

stant with height in the upper 80% of the mixed layer, and decreases only very slowly with height in the internal-wave region above z_i.

The earlier model with the lid at z_i (D1) produced strong peaks in both the horizontal velocity variance and pressure fluctuation at $z=z_i$ which are seen to be absent when the lid is removed. Evidently, most of the kinetic energy of the overshooting updrafts near $z=z_i$ is consumed in forcing the entrainment rather than in the conversion to horizontal kinetic energy. Part is also consumed in the forcing of the internal waves above z_i.

The normalized temperature variance is shown in Figure 6 for the same four times during DAY 33. The curves agree rather closely in the lower 80% of the mixed layer, while a secondary maximum centered at $z/z_i=1.1$ grows and dominates in the upper

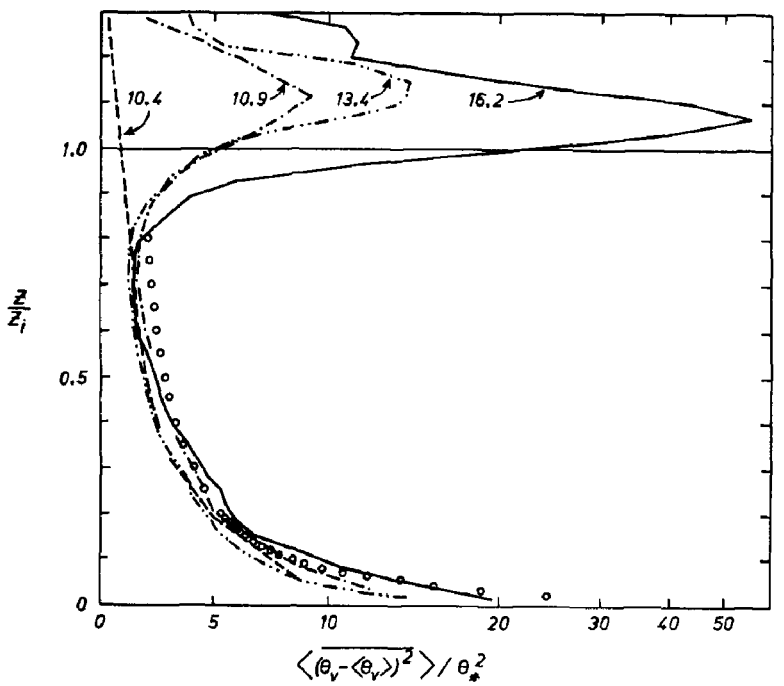

Fig. 6. Vertical profiles of dimensionless virtual-potential-temperature variance calculated for the four designated times. Abscissa changes from linear to logarithmic at 10.

portion. This secondary maximum is associated with the development of increased stratification at $z=z_i$, as well as with the development of increasingly energetic internal waves. Hence, the temperature variance in the vicinity of $z=z_i$ cannot be expected to scale with θ_*^2. The variance in this region contrasts sharply with the continued decrease with height found in a model with a lid at z_i (see D1).

The circles in Figure 6 represent the formula

$$\langle(\theta-\langle\theta\rangle)^2\rangle/\theta_*^2 = 1.8(z/z_i)^{-2/3} \tag{3}$$

of Wyngaard *et al.* (1971) which apparently holds quite well up to $z=0.4\ z_i$, and holds approximately even up to $z=0.8\ z_i$. However, in the surface layer at $z=0.02\ z_i$, the average of the numerically calculated values is about 30% smaller than what Equation (3) gives. If valid, this result might be due to the effect of significant horizontal variations of surface temperature which occur at the most uniform of land sites but were non-existent in the model. The discrepancy could be expected to be even greater if the micrometeorological formula had been derived from horizontal averages instead of from time averages.

The normalized specific-humidity variance is shown in Figure 7. With the exception of hour 10.9, the curves agree closely with each other in the lower half of the mixed layer. As with the temperature variance, however, they cannot agree in the upper portion where the very large values are associated not with surface-layer processes but with a negative humidity gradient at and just above z_i which had become quite significant by hour 11 and which increased thereafter (see D2, Figure 2). Between hours

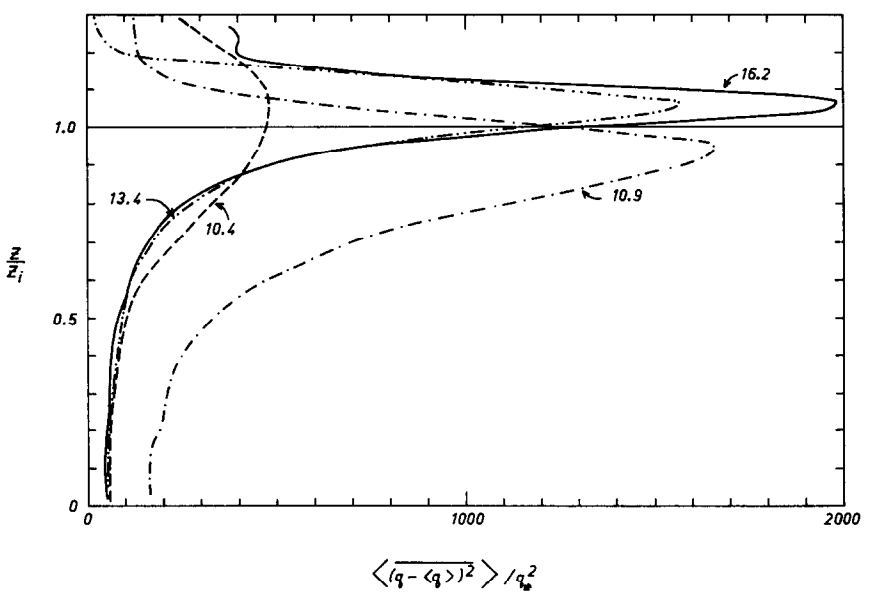

Fig. 7. Vertical profiles of dimensionless specific-humidity variance calculated for the four designated times.

10.4 and 10.9 the calculated mixed layer thickened very rapidly as the thermal plumes rose through an essentially adiabatic region, and a great quantity of dry air was then entrained. There is little doubt that the anomalously large entrainment rate immediately preceeding hour 10.9 caused the anomalously large humidity variance at hour 10.9 shown in Figure 7. However, the close agreement between the other three curves for $z \leqslant 0.3\ z_i$ must be somewhat fortuitous, as they have a distinctly different value and vertical gradient in and near the surface layer than does the normalized temperature

variance. This result suggests that even in the surface layer, the humidity variance was largely controlled by the entrainment process at $z=z_i$. This conclusion is discussed further in the next section.

The relatively huge humidity variances near $z=z_i$ in Figure 7, after hour 10.4, might be thought to be erroneous. However, the standard deviation at $1.06\,z_i$ at hour 16.2, for example, was $(\sigma_q)_{\max}=0.48\times10^{-3}$. At that time, the drop in calculated specific humidity between the heights 1400 and 1600 m was 1.5×10^{-3} (see D2). Hence the smaller value of $(\sigma_q)_{\max}$ obtained here does not seem at all unreasonable. Nevertheless, it would be interesting to have aircraft humidity measurements taken under similar conditions (using horizontal flight paths) for comparison.

The correlation coefficients for the covariances $\langle\overline{w\theta_v}\rangle$, $\langle\overline{wq}\rangle$, and $\langle\overline{\theta''_v q''}\rangle$ (horizontal mean values are removed from variables with a double-prime superscript) are shown in Figure 8 which applies to hour 14. Of interest is the relatively great height interval $(0<z<0.6z_i)$ over which the heat-flux correlation coefficient remains near or above 0.5,

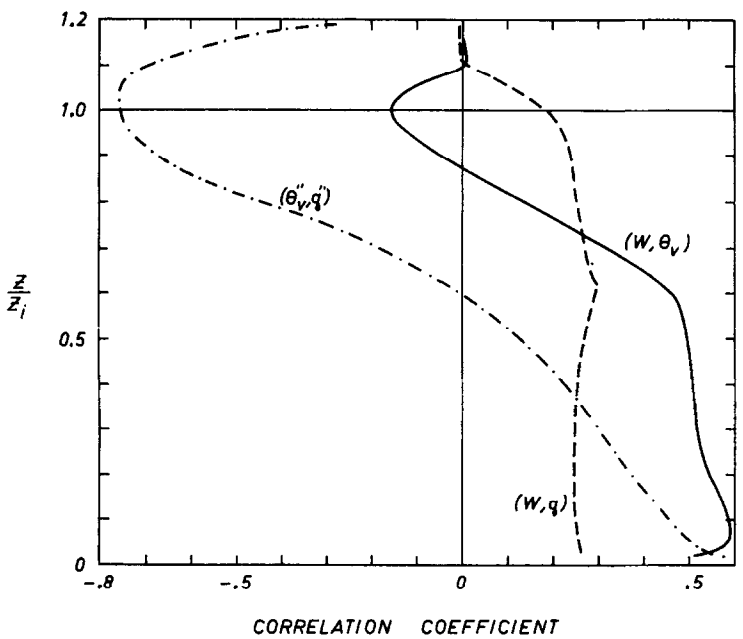

Fig. 8. Vertical profiles of the correlation coefficients between w and θ_v, between w and q, and between θ''_v and q'' at hour 14 (horizontal mean values are removed from variables with a double-prime superscript.)

the relatively constant value of the moisture-flux correlation coefficient, and the large negative correlation coefficient for $\langle\overline{\theta''_v q''}\rangle$ in the upper portion of the mixed layer. In the latter region, the warmest air coincides with the dry air entraining into the mixed layer, whereas in the lower part of the mixed layer, the warmest air is found in the plumes which are relatively moist.

Correlation coefficients for the momentum fluxes were very small and are not shown here. They were generally less than 0.1 in magnitude throughout the mixed layer.

Skewness coefficients for vertical velocity ($S_w = \langle \bar{w}^3 \rangle / \langle \bar{w}^2 \rangle^{3/2}$) and for $\bar{\theta}_v$ and $\bar{q}$ (similarly defined and denoted by S_θ, S_q) are shown in Figure 9 for hour 16.9. (This time was still sufficiently before sunset for the heat flux to have its characteristic vertical profile.) The skewness coefficients provide some idea of how fluctuations of a given sign may be preponderant. These involve only that portion of the skewness asso-

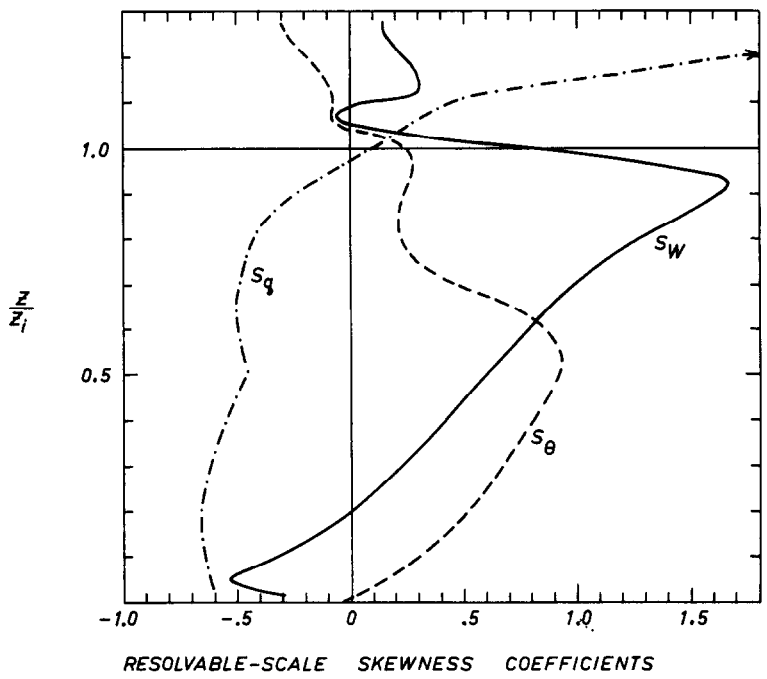

Fig. 9. Vertical profiles of skewness coefficient for vertical velocity S_w, for virtual potential temperature, S_θ, and for specific humidity, S_q, at hour 16.9.

ciated with the resolvable-scale fluctuations, which may explain the lack of large positive values for S_w and S_θ near the surface. The negative values of S_q throughout almost all the mixed layer suggest that dry air entraining from $z = z_i$ becomes stretched into somewhat narrow streamers lower down, which then occupy but a small fraction of the area. The maximum positive value of S_w near z_i suggests that relatively strong upward motion in a relatively small number of active plumes dominates this statistic in the upper portion of the mixed layer. S_θ is not similarly explained in this region, probably because potentially warm air occupies not only the cores of the plumes but also various regions of downward entrainment existing outside the plumes.

The conclusions of this section are somewhat uncertain to the extent that the total variance of a quantity includes the subgrid-scale contribution. The fraction of the variance residing on the subgrid scale at hour 14.056 for momentum, temperature and

moisture is shown in Figure 10. The subgrid fraction for the velocity components is seen to become tolerably small above $0.06\, z_i$. The subgrid fraction for a horizontal velocity component, unlike that for the vertical component, does not approach unity as $z \to 0$ because of the low-level maximum in the resolvable-scale horizontal velocity components associated with plume inflows (see Figures 2 and 3).

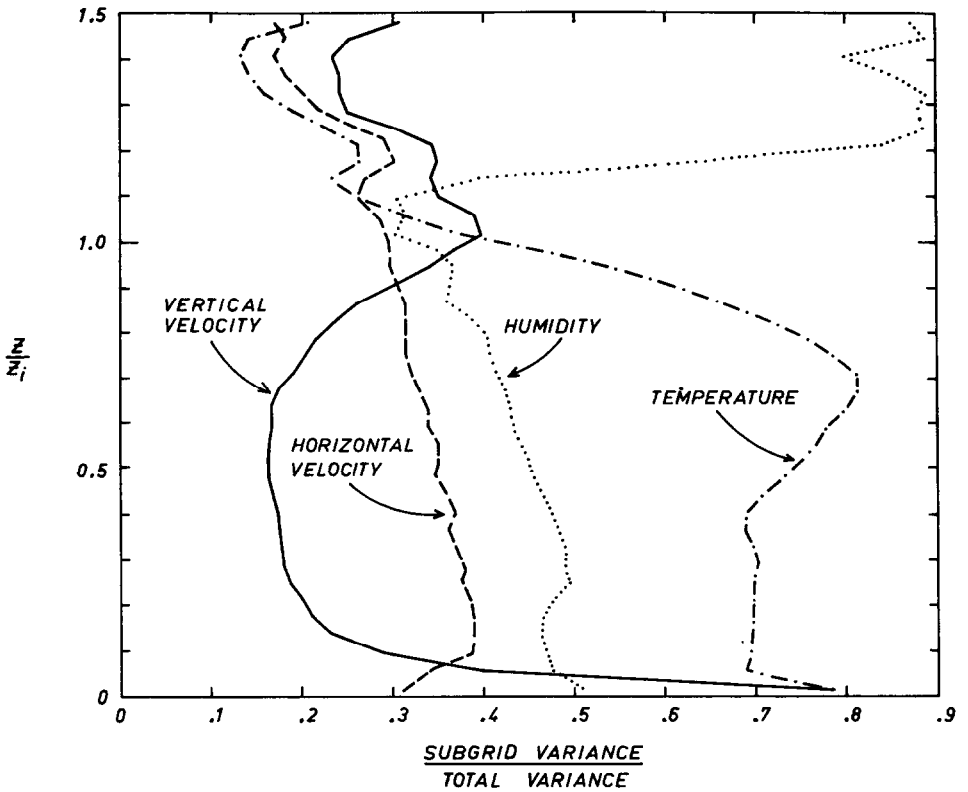

Fig. 10. Vertical profiles of the ratio of the subgrid variance to the total variance for vertical velocity, for a horizontal velocity component, for specific humidity, and for virtual potential temperature at hour 14.056.

The large subgrid fraction for temperature variance throughout the mixed layer comes as a surprise. However, it is apparently necessary; otherwise the calculated total temperature variance (see Figure 6) would not display approximately the observed value and profile shape, especially in the surface layer. The general agreement of that profile with aircraft measurements of Lenschow (1970) and Telford and Warner (1964), which have been plotted in D1, provides rough support therefore for the subgrid closure constants used in this study in the equations for the subgrid temperature and humidity variances. In the earlier model which used subgrid eddy coefficients (see D1), it was not clear how the subgrid temperature variance should be estimated. This ambiguity is resolved with the use of the full set of subgrid covariance equations (see D2).

The subgrid fraction of the humidity variance, $\langle \overline{q'^2} \rangle$, shown in Figure 10 behaves quite differently from that of temperature although the two subgrid equations are exactly similar. This result merely reflects the very different shapes of the respective vertical fluxes and spectra on the resolvable scale (to be discussed in Section 4) which arise from the opposite signs of the vertical gradients of $\langle \theta_v \rangle$ and $\langle q \rangle$ just above z_i.

The reason for the abrupt increase of the subgrid specific-humidity fraction above 1.1 z_i is unknown. However, the subgrid humidity variance is a completely passive quantity in that its value is not utilized in any other equation of the numerical computations.

The subgrid fraction of the pressure fluctuation has not been estimated here. As can be seen later when the spectra for pressure are presented, this subgrid fraction must be quite small.

The contribution of the horizontally averaged subgrid vertical *fluxes* towards the total mean vertical *fluxes* was found to be much smaller generally (see D2) than for the variances in Figure 10, above the lowest two vertical grid intervals.

3. Balance Equations for the Second Moments

The various terms in the turbulence kinetic energy balance, centered near hour 14, are shown in Figure 11 as a function of z/z_i. In this and the other budgets, the quantities are averages over three realizations of the turbulence spaced about three minutes apart. The terms in Figure 11 are made dimensionless by w_*^3/z_i, with the result that the buoyancy term, when dimensionless, has unit value as $z \to 0$. In the familiar dimensional form, this equation is

$$\frac{\partial}{\partial t}\langle \overline{u_i''^2/2} \rangle = -\langle \overline{uw} \rangle \frac{\partial \langle \tilde{u} \rangle}{\partial z} - \langle \overline{vw} \rangle \frac{\partial \langle \tilde{v} \rangle}{\partial z} + \frac{g}{\theta_v} \langle \overline{w\theta_v} \rangle - \frac{\partial}{\partial z} \langle \overline{w(u_i''^2/2 + p/\langle \varrho \rangle)} \rangle - \varepsilon , \tag{4}$$

where

$$u_i''^2 = (u_i - \langle u_i \rangle)(u_i - \langle u_i \rangle); \quad i = 1, 2, 3,$$

and the other terms have their usual meanings (summation is implied here for $u_i''^2$). The time-derivative term was negligible, as were the wind-shear terms except below the lowest grid interval. The rate of dissipation, ε, was obtained from the assumption used for it on the subgrid scale:

$$\varepsilon = 0.70 \langle E^{3/2} \rangle / \Delta , \tag{5}$$

where E is the subgrid turbulence kinetic energy and Δ is the representative grid interval (cube-root of the grid volume). The resolvable portion of the term $-\partial/\partial z \langle \overline{wp}/\langle \varrho \rangle \rangle$ was obtained directly and is labelled 'pressure-diffusion term'. Its subgrid-scale counterpart and the rest of the diffusion term (4th term on the right of Equation (4)) were obtained as a single residual.

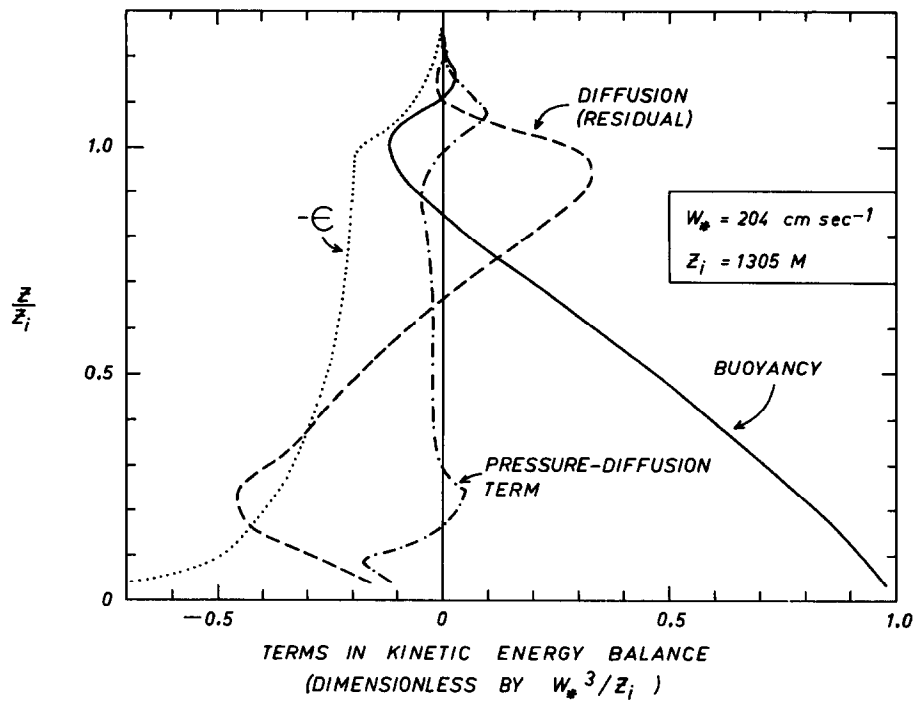

Fig. 11. Vertical profiles of terms in the turbulence kinetic energy budget, made dimensionless by w_*^3/z_i, at hour 14.1.

The undifferentiated resolvable-scale quantity $\langle \bar{p}\bar{w} \rangle / \langle \varrho \rangle$, normalized by w_*^3, is of some interest and is thus presented in Figure 12. A smoothed curve like that in this figure was used in obtaining the vertical derivative shown in Figure 11. At and above z_i, the positive values of $\langle \bar{p}\bar{w} \rangle$ are consistent with an export of energy from the mixed layer to the internal waves.

The assumption often made for $\langle \bar{p}\bar{w} \rangle$ is that it has the same sign as $-\partial/\partial z \langle \bar{w}^2 \rangle$. However, the latter quantity changed sign from − to + at $z = 0.3\, z_i$, whereas $\langle \bar{p}\bar{w} \rangle$ is seen to remain negative until $0.8\, z_i$. In this case, such an assumption would be too poor to warrant plotting in Figure 12.

The strange shape of $\langle \bar{p}\bar{w} \rangle$ below $0.3\, z_i$ is responsible for the equally strange shape of the resolvable pressure-diffusion term in this region in Figure 11. It is possible that below 0.2 or $0.3\, z_i$, the unknown subgrid-scale portion of the pressure-diffusion term is positive and dominates. Then, the portion of the diffusion term not associated with pressure might, as expected, be most negative in the surface layer (Wyngaard and Coté, 1971), thereby explaining why the residual curve in Figure 11 bends back toward zero in this region. An alternative explanation for the latter behaviour is that the subgrid portion of the diffusion term is in large error in the region $z < 0.2\, z_i$ because of the down-gradient type of tensor-invariant assumption utilized in the model (see D2). As has been pointed out by Wyngaard (1973), that assumption, at

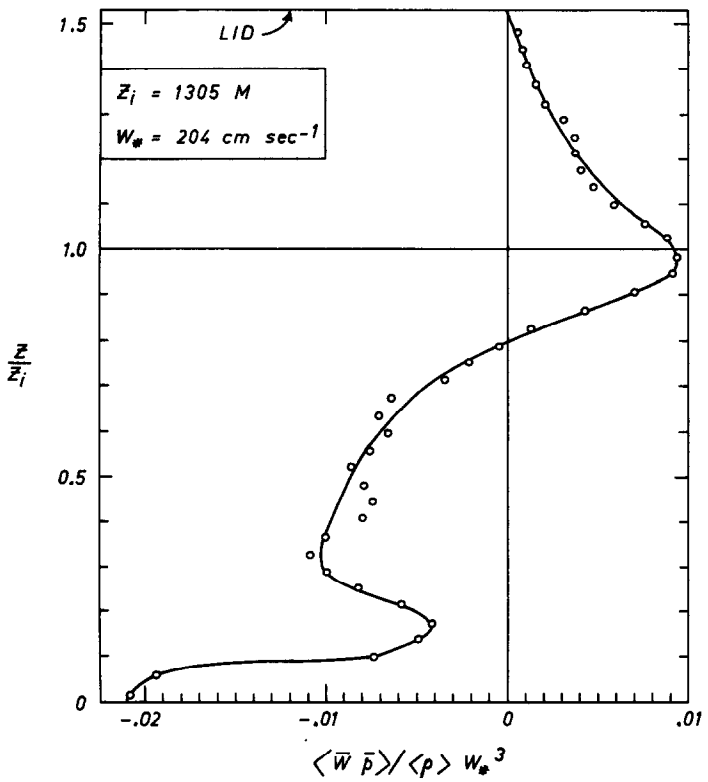

Fig. 12. Vertical profile of $\langle \bar{w}\bar{p} \rangle$, normalized by $\langle \varrho \rangle w_*^3$, at hour 14.1.

least as applied to $\langle w^3 \rangle$, is incorrect even in sign in the unstable surface layer. Consequently, ε and the subgrid turbulence energy could both be somewhat too small if the vertical integral of a corrected diffusion term were to vanish.

It must be pointed out that the vertical integral of a diffusion term obtained as a residual in this and the other second-moment equations does not necessarily vanish. The resolvable-scale portions of some of the terms involved, when obtained in the simplest fashion, are not entirely compatible with their counterparts which would be obtained by multiplying the appropriate prognostic finite-difference equation by the appropriate resolvable-scale variable and averaging horizontally. That is because of the finite-difference scheme used for the non-linear terms, involving a space-staggered grid network.

The curves in Figure 11 in the region $0.3 < z/z_i < 1$ are very similar to those obtained by Lenschow (1970, 1974) from aircraft measurements, and to those of Willis and Deardorff (1974) from a laboratory convection tank. In the upper part of the mixed layer, the diffusion term is seen to be most positive and the only source to maintain the turbulence against the losses due to dissipation and negative heat flux. Even in this region, the wind-shear source terms were negligibly small on DAY 33.

The terms in the virtual potential-temperature variance balance equation are shown in Figure 13. This equation is

$$\frac{\partial}{\partial t}\langle(\theta_v - \langle\theta_v\rangle)^2\rangle = -2\langle\overline{w\theta_v}\rangle\frac{\partial\langle\bar{\theta}_v\rangle}{\partial z} - \frac{\partial}{\partial z}\langle\overline{w(\theta_v - \langle\theta_v\rangle)^2}\rangle - \chi, \tag{6}$$

where the molecular destruction term, χ, was obtained from its subgrid assumption:

$$\chi = 0.42\left\langle\frac{E^{1/2}}{\Delta}\overline{\theta_v'^2}\right\rangle. \tag{7}$$

Here, E and $\overline{\theta_v'^2}$ are the subgrid portions of the turbulence energy and virtual potential-temperature variance. The diffusion term (second term on the right of Equation (6)) was obtained as a residual again, and is seen to be of dominant importance above the surface layer, as expected. It is the only source term in the region where the production term is slightly negative or the lapse rate essentially adiabatic. The large value of the production term centered at $z/z_i = 1.04$ in Figure 13 is responsible for the large temperature variance at this height discussed in connection with Figure 6.

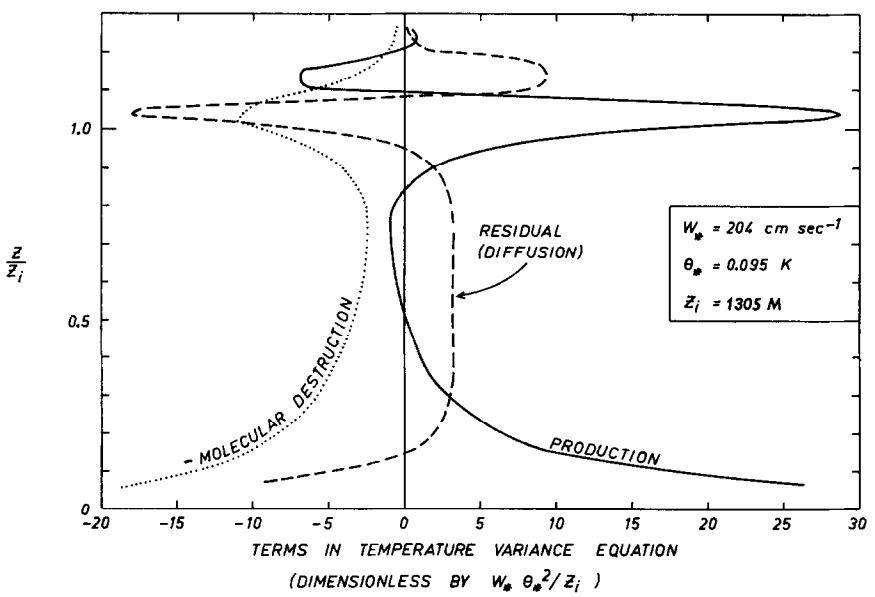

Fig. 13. Vertical profiles of terms in the virtual-potential-temperature variance equation, made dimensionless by $w_*\theta_*^2/z_i$, at hour 14.1.

The only feature that appears unrealistic in Figure 13 is the negative value of the production term centered at $z/z_i = 1.13$, where the heat flux had a tiny positive, or countergradient, value (see the buoyancy-term profile of Figure 11). However, the weak positive heat flux here existed on both the resolvable and subgrid scales, and is therefore difficult to ascribe to a model error.

The terms in the moisture-variance equation, which is exactly analogous to Equation (6) with q replacing θ_v, are shown in Figure 14. The subgrid assumption for the molecular-destruction term was also analogous to Equation (7). The region of large production aloft in the mixed layer is seen to be very extensive, and is responsible for the failure of the humidity variance profile to be similar to the temperature-variance profile in the lower portion of the mixed layer as well as aloft. The fact that the mois-

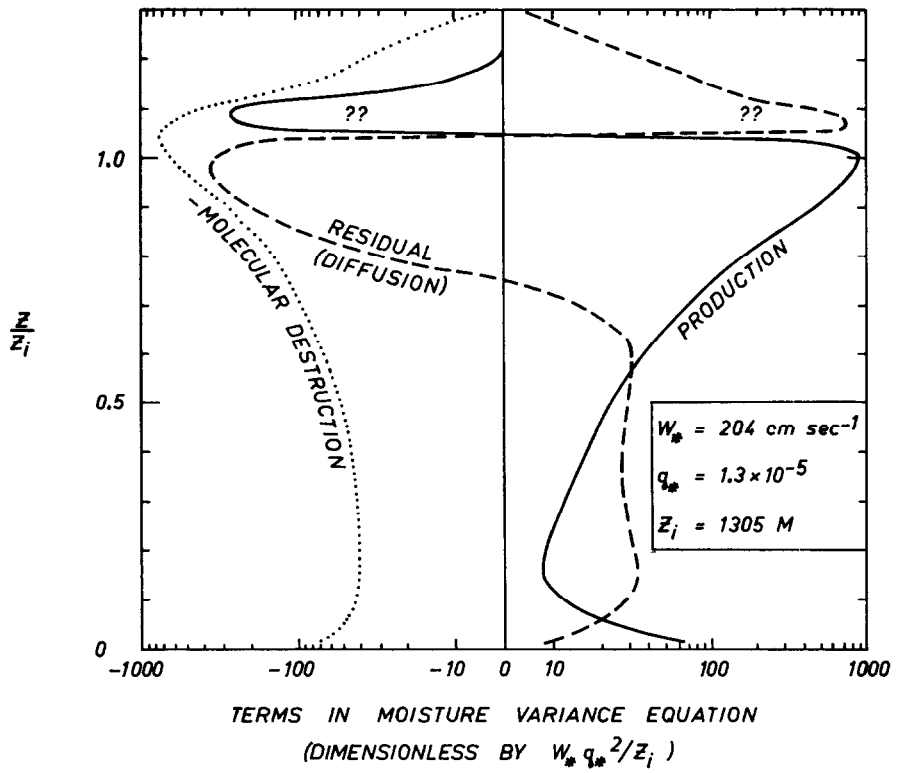

Fig. 14. Vertical profiles of terms in the specific-humidity variance equation, made dimensionless by $w_* q_*^2 / z_i$, at hour 14.1. Abscissa changes from linear to logarithmic at ± 10.

ture flux did not diminish with height on DAY 33 until a height of nearly z_i is reached (see D2) is in turn responsible for the entrainment effect dominating the humidity-variance production term to a height as small as $0.17\, z_i$ at hour 14. The effect of the surface moisture flux is seen to have dominated that term only below about $0.17\, z_i$. Turbulent diffusion of q^2 then caused the entrainment effect to influence strongly the humidity variance even in the surface layer. One should only expect the humidity variance, as normalized by q_*^2, to behave like the similarly scaled temperature variance if the ground were considerably more moist, or the air aloft not so dry, as on DAY 33. Such anomalous behavior does not occur with the virtual potential-temperature variance in the surface layer or lower mixed layer because the vertical profile of

$\langle w\theta_v\rangle/\langle w\theta_v\rangle_{sfc}$ maintains a unique shape throughout the lowest 85% of a well mixed layer.

A spurious feature of Figure 14 appears to be the relatively large negative value of the production term centered at $z = 1.09\ z_i$, as discussed in D2 and later in this paper. It occurred only on the subgrid scale.

The terms in the sensible heat-flux balance equation are shown in Figure 15. This equation is

$$\frac{\partial}{\partial t}\langle\overline{w\theta_v}\rangle = -\langle\overline{w^2}\rangle\frac{\partial\langle\bar{\theta}_v\rangle}{\partial z} + \frac{g}{\theta_v}\langle\overline{(\theta_v - \langle\theta_v\rangle)^2}\rangle - \frac{\partial}{\partial z}\langle\overline{w^2(\theta_v - \langle\theta_v\rangle)}\rangle - \\ - \frac{\partial}{\partial z}\left\langle\overline{\left(\frac{p - \langle p\rangle}{\langle\varrho\rangle}\right)(\theta_v - \langle\theta_v\rangle)}\right\rangle + \left\langle\overline{\left(\frac{p - \langle p\rangle}{\langle\varrho\rangle}\right)\frac{\partial\theta_v}{\partial z}}\right\rangle. \tag{8}$$

The first term on the right is the production term, the second is the buoyancy term, the third and fourth are the vertical-velocity and pressure diffusion terms, respectively, and the last is here called the 'pressure-correlation' term. The latter, when split into the resolvable- and subgrid-scale portions, is

$$\left\langle\overline{\left(\frac{p - \langle p\rangle}{\langle\varrho\rangle}\right)\frac{\partial\theta_v}{\partial z}}\right\rangle = \left\langle\left(\frac{\bar{p} - \langle\bar{p}\rangle}{\langle\varrho\rangle}\right)\frac{\partial\bar{\theta}_v}{\partial z}\right\rangle - \\ - \left[4.13\left\langle\frac{E^{1/2}}{\Delta}\overline{w'\theta_v'}\right\rangle + \frac{1}{3}\frac{g}{\theta_v}\langle\overline{\theta_v'^2}\rangle\right] \tag{9}$$

where the second term on the right constitutes the subgrid assumption utilized in this model. The diffusion terms were obtained as a single residual, which agrees qualitatively with the circles denoting the surface-layer formulation for $-\partial/\partial z\,\langle w^2(\theta_v - \langle\theta_v\rangle)\rangle$ recommended by Wyngaard *et al.* (1971). This rough agreement is probably the most that can be expected close to the surface layer, since the choice of the subgrid closure constants used herein had no input from surface-layer measurements except for assuring that their values were compatible with a critical Richardson number of value 0.21.

The buoyancy term in Figure 15 is seen to be of paramount importance at all heights, especially in the upper part of the mixed layer where the gradient production term is strongly negative.

Regarding the pressure-correlation term in Figure 15, the subgrid portion is seen to dominate the resolvable-scale portion in the mixed layer, probably because of the similar dominance of the subgrid temperature variance over the resolvable temperature variance (see Figure 10). Thus, the fact that the subgrid assumption gives a profile of similar shape and sign as the profile of the resolvable portion above the surface layer is reassuring.

The terms in the moisture-flux budget equation at hour 14.1 are shown in Figure 16. The equation is the same as in Equations (8), (9) if q replaces θ_v everywhere (except only once in the buoyancy term). The dominance of terms in the upper portion of the mixed layer, as opposed to the lower portion, is the most outstanding feature. The

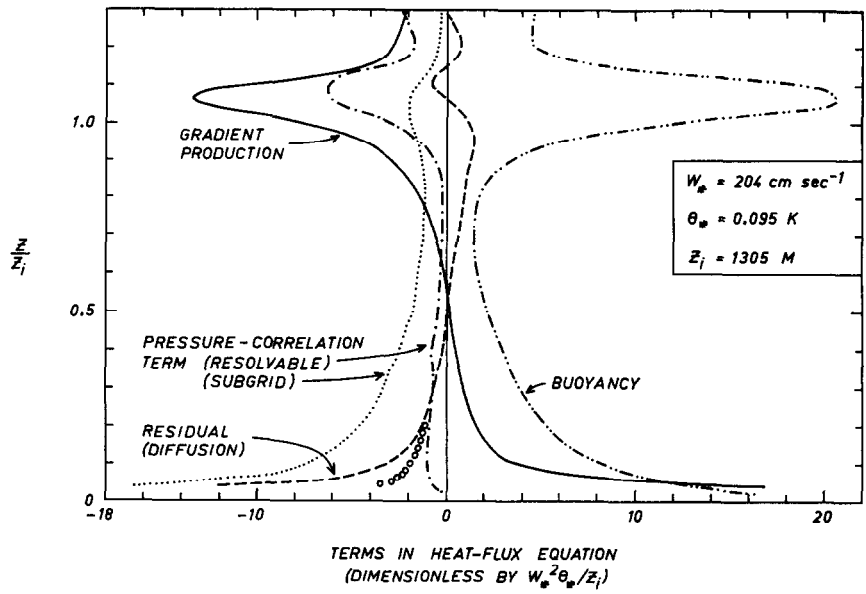

Fig. 15. Vertical profiles of terms in the budget equation for $\langle \overline{w\theta_v} \rangle$, made dimensionless by $w_*^2\theta_*/z_i$, at hour 14.1.

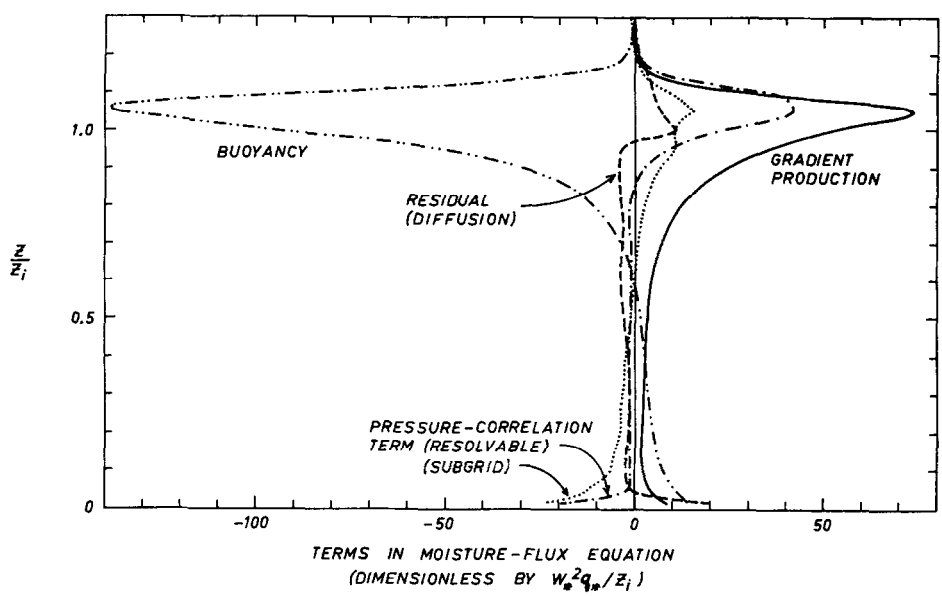

Fig. 16. Vertical profiles of terms in the budget equation for $\langle \overline{wq} \rangle$, made dimensionless by $w_*^2q_*/z_i$, at hour 14.1.

gradient production term, in this case, is positive throughout the mixed layer because $\partial\langle q\rangle/\partial z$ has the same sign (negative) at the top of the mixed layer as it has in the surface layer. On the other hand, the buoyancy term switches sign in the middle of the mixed layer in accordance with the $\theta_v - q$ correlation curve of Figure 8. Its large negative value in the upper mixed layer allows $\langle\overline{wq}\rangle$ to reach near-equilibrium values despite the large positive gradient-production term there.

4. Spectra Along Horizontal Lines

Discrete line spectra calculated at four different heights relative to z_i are shown in Figures 17 and 18. Each is an average of 20 individual spectra along lines separated by 2 Δx or 2 Δy, and is also an average of 10 separate realizations spaced about 3 min apart in time and centered at hour 14. Nearly this much averaging (equivalent to perhaps 100 5-km pathlengths at each height) appears necessary to remove secondary

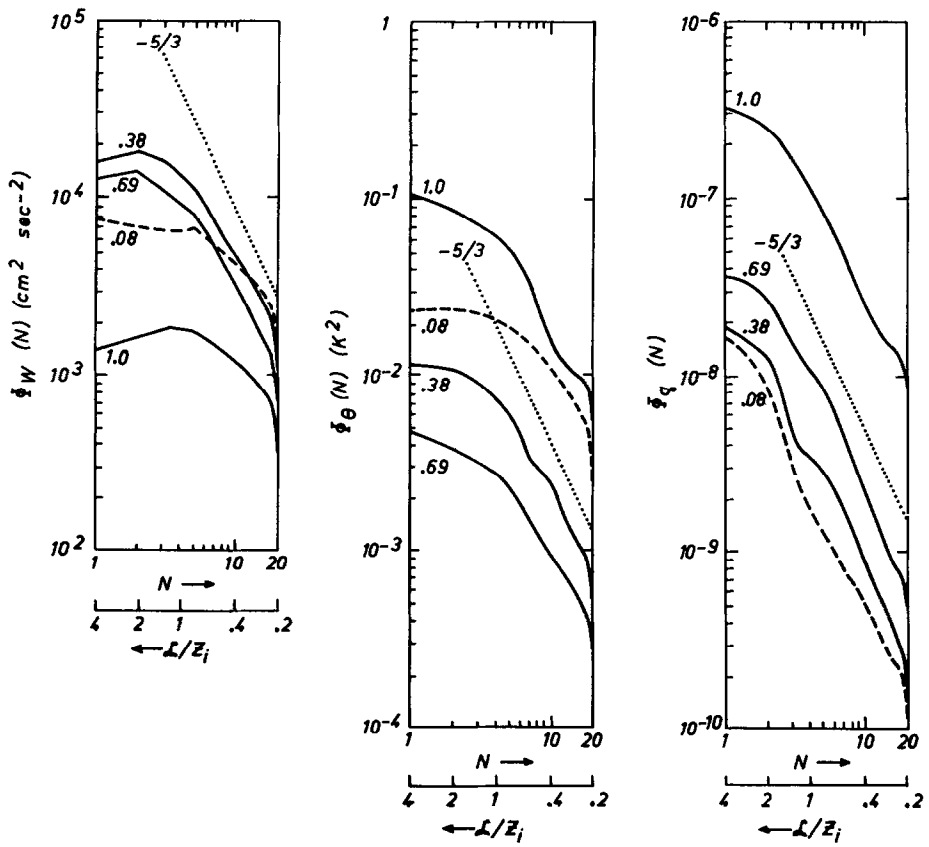

Fig. 17. Averaged horizontal line spectra (at discrete wave numbers N) for vertical velocity, Φ_w; for virtual potential temperature, Φ_θ; and for specific humidity, Φ_q; centered at hour 14, for the four heights $z/z_i = 0.08$, 0.38. 0.69, and 1.0. The normalized wavelength, $\mathscr{L}/z_i$, is given by 5 km/($N z_i$).

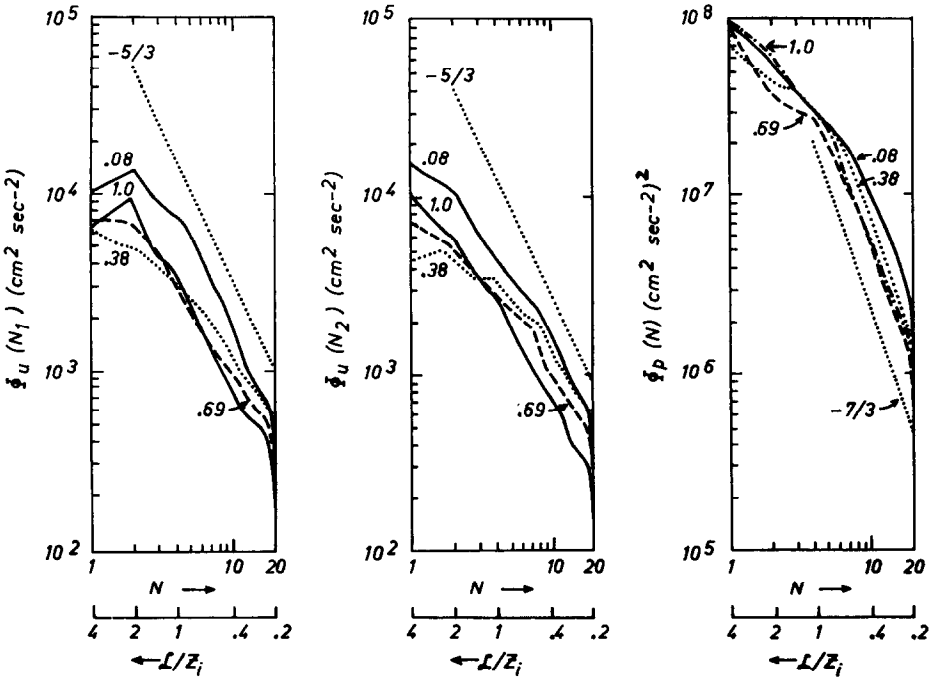

Fig. 18. Averaged horizontal line spectra (at discrete wave numbers N) for $\bar{u}$ along x or $\bar{v}$ along y, $\Phi_u(N_1)$; for $\bar{u}$ along y or $\bar{v}$ along x, $\Phi_u(N_2)$; and for pressure / $\langle\varrho\rangle$, $\Phi_p(N)$, at the four indicated heights at hour 14.

peaks which can otherwise occur and be mistaken as real features. Only 20 wave-numbers (N) are available because of the use of only 40 grid intervals along x or y. Wave number $N=1$ corresponds to 5 km and $N=20$ corresponds to 250 m. The spectral estimates $\Phi(N)$ shown here have the property that $\sum_1^{20}\Phi(N)$ equals the resolvable scale variance along a line. To convert to the more conventional representation per unit wave number, the spectral ordinates shown here should be multiplied by 5 km $(2\pi)^{-1}$, and the abscissa N by $2\pi\,(5\text{ km})^{-1}$.

The spectra of Figure 17 represent the average of spectra along both x and y lines. The vertical-velocity spectrum, Φ_w, at $z/z_i=0.08$ contains relatively more energy in the higher wave numbers than do the next two higher levels, 0.38 and 0.69. At the latter two heights, however, there is a definite maximum, in this log-log type plot, at a wavelength $\mathscr{L}=2\,z_i$, which agrees approximately with aircraft measurements of Lenschow (1970). A spectral slope close to $-5/3$ there appears to commence at $\mathscr{L}/z_i=$ 0.6. At $z/z_i=1.0$, the spectral maximum is shifted, surprisingly, to a smaller wavelength of about z_i, with no hint of the beginnings of an inertial subrange out to $\mathscr{L}/z_i$ of 0.2. In all cases the spectral estimates for $N=20$ appear too low by a factor of 2, probably because they contain only the 2 Δx, or cosine, wave.

The scaling of $\mathscr{L}$ with z_i in the case of Φ_w was very apparent in the numerical calcu-

lations. Early in the simulation of DAY 33, when z_i was only about 150 m, the $2\,\Delta x$ wave (of length 250 m) was very dominant.

The temperature spectra, $\Phi_\theta(N)$, and specific-humidity spectra, $\Phi_q(N)$, display quite different shapes for $\mathscr{L}/z_i > 0.5$ to 0.8. The former begins to flatten out in this region while the latter does not until a wavelength of at least $2\,z_i$ is reached. The difference is most striking at the lowest height despite the strong positive correlation between θ_v and q there (see Figure 8). The greater subgrid variance fraction for temperature than for humidity (Figure 10) is associated with this phenomenon. It appears quite evident that it is associated with the entrainment of dry but warm air downward at locations in between the warm, moist plumes. This breaks up the temperature field into smaller-scale features but preserves the longer wavelengths of the moisture field (see also Figure 4). Qualitatively the same behavior has been observed in the marine subcloud layer by Phelps and Pond (1971). However, it is puzzling that they found this phenomenon in their measurements near the Barbados but not near San Diego. It is possible that during the latter measurements, the entrainment at the top of the marine layer was either very weak, or the air there had little moisture contrast, or both.

The spectra $\Phi_u(N_1)$, averaged with $\Phi_v(N_2)$, are shown in the left of Figure 18; and those of $\Phi_u(N_2)$ averaged with $\Phi_v(N_1)$ are shown in the center. Here, N_1, N_2 correspond to wave numbers along the x, y axes, respectively. At the higher wave numbers where the spectral slopes are suggestive of an inertial subrange, the lateral velocity spectra at intermediate heights average about 1.1 of the longitudinal, whereas the isotropic value of this ratio is 4/3. On the other hand, the earlier model which used subgrid-scale eddy coefficients gave a value of about 2 for this ratio (Deardorff, 1972b). Evidently, this statistic is quite model dependent.

The spectra of pressure, $\Phi_p(N)$, on the right of Figure 18 (averages along both x and y lines), show little variation with height except for larger values at the lowest levels for $N > 5$. At the upper three of the four heights, the spectral slope in this wave-number region is close to the $-7/3$ expected in an isotropic inertial subrange (Batchelor, 1953, p. 183). However, the spectral slopes obtained here should not be scrutinized too quantitatively. Not only is there a great shortage of wave numbers, but one would expect a gradual steepening of the spectra of the grid-volume averaged variables in the apparent inertial subrange before wave number 19 is reached. The absence of this steepening suggests that some further revision of some of the subgrid closure constants may become necessary, and/or an improved spatial finite-difference scheme having less truncation error at high wave numbers.

Most of the spectra of Figure 18 indicate increasing variance with decreasing wave number, suggesting that a larger domain of integration (or larger grid interval) would be desirable. This is especially true for humidity and for the horizontal velocity components. Numerically derived values of the variances of the latter have been noticed by H. Panofsky (private communication) to be smaller than observed. The discrepancy appears to be on the order of 50%, and indeed associated with wavelengths greater than roughly 5 km. On the other hand, the substantial, or in some cases large, subgrid variance fractions (Figure 10) suggest that a smaller grid interval is desirable

instead; at the least, they suggest that a sophisticated treatment of the subgrid stresses and fluxes is appropriate.

5. Assumption for Pressure-Correlation Terms

Examination of the correlations of the resolvable-scale pressure fluctuations with the vertical gradients of velocity, temperature or moisture may shed some light on turbulence closure assumptions appropriate for one-dimensional models. For such a model, the Rotta (1951) type assumption is

$$\left\langle \frac{p''}{\langle \varrho \rangle} \left(\frac{\partial u_i}{\partial x_j} + \frac{\partial u_j}{\partial x_i} \right) \right\rangle = - c_M \frac{\mathscr{E}^{1/2}}{l} \left[\langle u_i'' u_j'' \rangle - \tfrac{2}{3} \delta_{ij} \langle \mathscr{E} \rangle \right], \tag{10}$$

where $\mathscr{E}$ is the total turbulence energy, l is the length scale

$$l = \mathscr{E}^{3/2}/\varepsilon \tag{11}$$

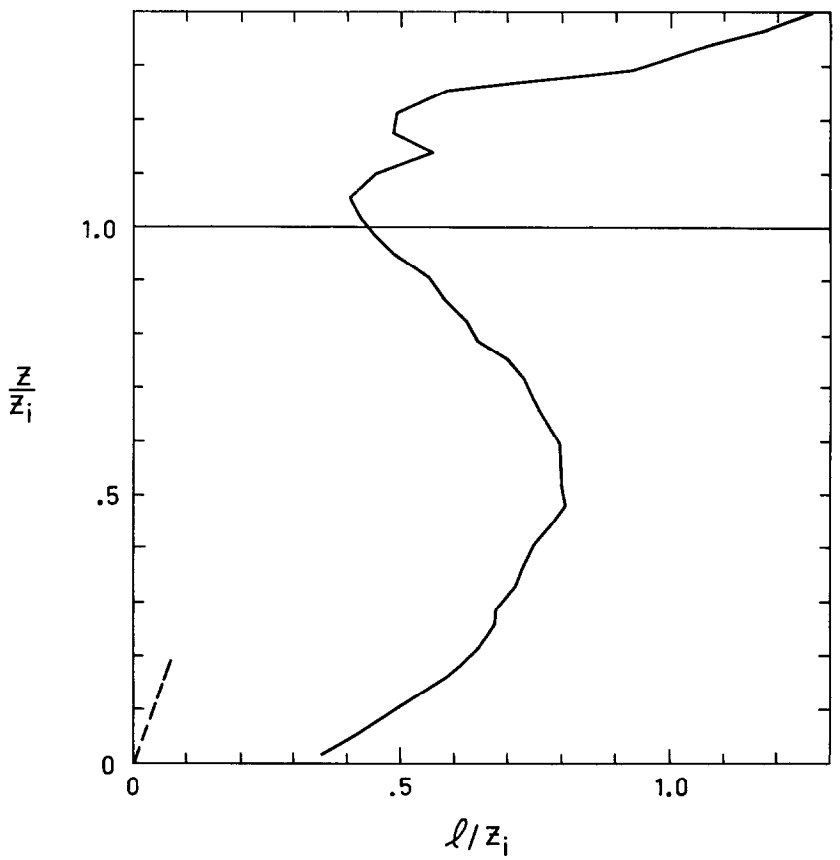

Fig. 19. Vertical profile of the dimensionless mixing length, $l/z_i = \mathscr{E}^{3/2}/\varepsilon z_i$, at hour 14.1.

and c_M is a constant. The profile found for l at hour 14.1 is shown in Figure 19. It has the same shape as that reported earlier (Deardorff, 1973), but unfortunately that profile was erroneously large by a factor of about 2. The dashed line in Figure 19 is the expected value of l/z_i for a *neutral* surface layer, assuming $\mathscr{E}=4\,u_*^2$ and $\varepsilon=u_*^3/(0.35\,z)$. The much larger calculated mixing length even at $z/z_i=0.02$ is to be expected in that even at this height (25 m) the value of $-z/L$ (about 20) greatly exceeded unity. The rapid increase of l above $z=1.2\,z_i$ is indicative of internal gravity waves containing kinetic energy but undergoing less and less diffusion or turbulent breakdown with increasing height.

Using the above profile for l, Equation (10) was tested for $i=j=3$:

$$2\left\langle \frac{\bar{p}''}{\langle\varrho\rangle}\frac{\partial \bar{w}}{\partial z}\right\rangle = -\,c_M\,\frac{\mathscr{E}^{1/2}}{l}\,\langle \bar{w}^2-\tfrac{2}{3}\bar{E}''\rangle \tag{12}$$

where $\bar{E}''$ is the resolvable-scale turbulence energy and the double-prime is used to denote the deviation from the horizontal average ($\bar{u}''=\bar{u}-\langle\bar{u}\rangle$, etc., and $\bar{E}''=\tfrac{1}{2}(\bar{u}''^2+\bar{v}''^2+\bar{w}''^2)$). The two terms of Equation (12) are shown in Figure 20 for hour 14.056. The value 3 has been chosen here for c_M as giving best average fulfillment of

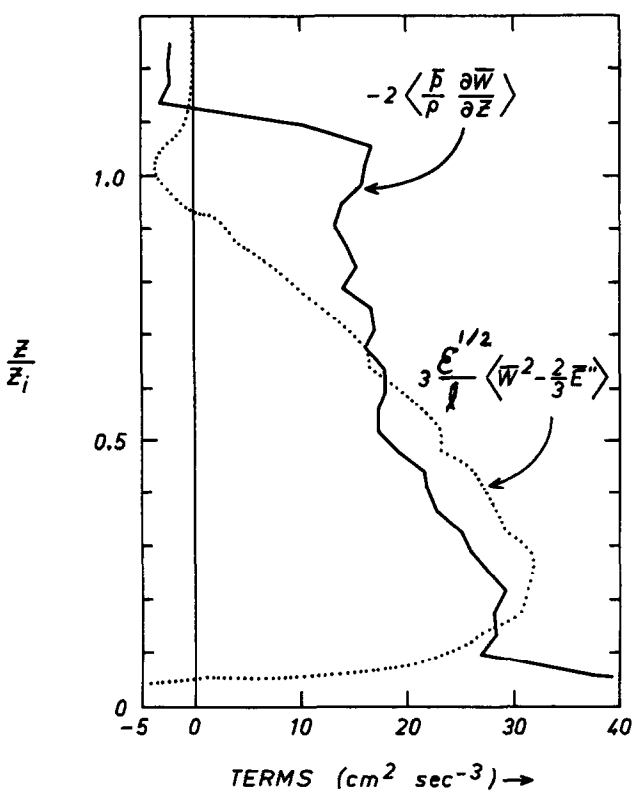

Fig. 20. Vertical profiles of $-2\langle(\bar{p}/\langle\varrho\rangle)\,\partial\bar{w}/\partial Z\rangle$ (solid curve) and an assumption for it (dotted curve), at hour 14.056.

Equation (12) in the interval $0.1 < z/z_i < 0.9$. The great disagreement in the two curves below $0.1\ z_i$ can perhaps be dismissed as due to vastly increased importance of subgrid-scale motions in this layer. However, the disagreement above $0.8\ z_i$ suggests that Equation (12) is rather inadequate. A better closure method (possibly that of Lumley and Khajeh-Nouri (1974)) may therefore be necessary for a one-dimensional model, if accuracy rather than simplicity is desired. Hopefully a more sophisticated method is not necessary in a detailed three-dimensional model if the grid volume is small enough to lie well within the inertial subrange at heights above the lowest grid interval.

The quantity $2\langle(\bar{p}/\langle\varrho\rangle)\,\partial\bar{w}/\partial z\rangle$ or equivalently, when $-z_i/L$ is very large, $2\langle(\bar{p}/\langle\bar{\varrho}\rangle)\times\partial\bar{v}/\partial y\rangle$, can also be obtained from Figure 20; either is then very closely given by $-\langle\bar{p}/\langle\varrho\rangle\,\partial\bar{w}/\partial z\rangle$. A curious aspect of the latter quantity is its similarity in shape and magnitude, in the mixed layer, to a variance of a horizontal velocity component multiplied by w_*/z_i (see Figure 5).

An assumption similar to that of Equation (12) but with vertical velocity on the left-hand side replaced by θ_v or by q is:

$$\left\langle \frac{\bar{p}''}{\langle\varrho\rangle}\frac{\partial\bar{\theta}_v}{\partial z}\right\rangle = -\,c_s\frac{\mathscr{E}^{1/2}}{l}\langle\bar{w}\bar{\theta}_v\rangle - a\,\frac{g}{\theta_v}\langle(\bar{\theta}_v'')^2\rangle \tag{13}$$

$$\left\langle \frac{\bar{p}''}{\langle\varrho\rangle}\frac{\partial\bar{q}}{\partial z}\right\rangle = -\,c_s\frac{\mathscr{E}^{1/2}}{l}\langle\bar{w}\bar{q}\rangle - a\,\frac{g}{\theta_v}\langle\bar{\theta}_v''\bar{q}''\rangle \tag{14}$$

The last term in either Equation (13) or (14) is a buoyancy compensation term arising from an exact treatment of the linearized Poisson equation for pressure, assuming isotropy and a constant resolvable-scale gradient over the grid interval. It is of the same nature as the Lilly (1967)-Crow (1968) strain-rate compensation term. The coefficient a was found by D. Taulbee (Dept. of Mechanical Eng., State College of New York, Buffalo, New York, unpublished notes) to be

$$a = 1/3 \tag{15}$$

Here, however, a is calculated from Equation (13) at the height $0.8\ z_i$ where $\langle\bar{w}\bar{\theta}_v\rangle$ crossed zero. The value found is

$$a = 0.38\,. \tag{16}$$

With this value in place of 1/3, c_S was obtained from Equation (14) at the height where the resolvable humidity-temperature covariance crossed zero ($z/z_i = 0.64$). The value found is

$$c_S = 1.14. \tag{17}$$

Using the above values for a and c_S, the pressure scalar-gradient correlation terms on the left-hand sides of Equations (13) and (14) are compared against the two right-hand assumed terms for hour 14.056 in Figures 21 and 22. It is immediately evident how important the buoyancy-compensation term is near the top of the mixed layer where the temperature and humidity variances and covariance are large. In the case

of Equation (13), however, the agreement would be improved if the coefficient a were only about 0.2 in the lower two-thirds of the mixed layer, increasing rapidly to about 0.4 near z_i. In the case of Equation (14), the agreement would be improved if $a=0$ in the lowest 80% of the mixed layer, increasing to about 0.47 at $z=1.06\,z_i$. A value

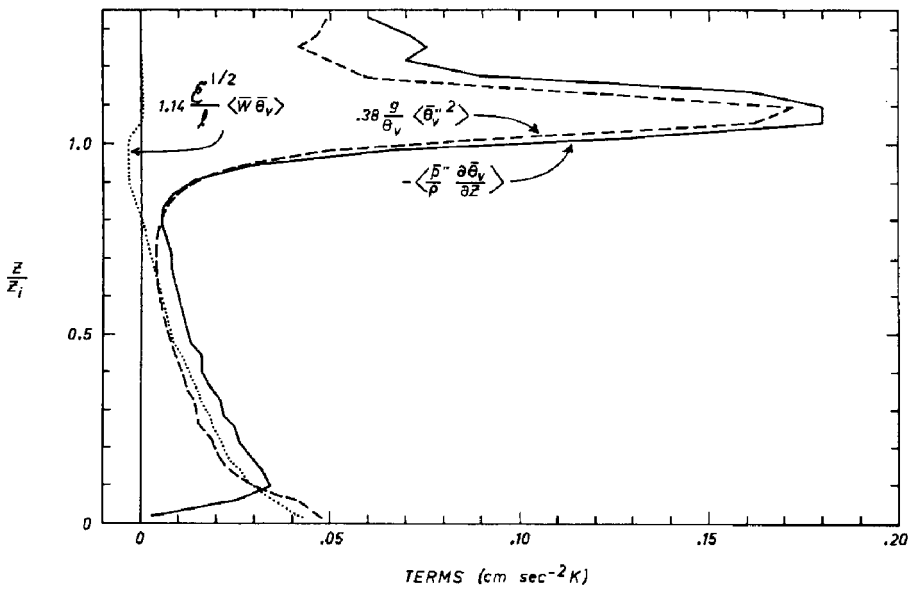

Fig. 21. Vertical profiles of $-\langle(\bar{p}''/\langle\varrho\rangle)\,\partial\bar{\theta}_v/\partial Z\rangle$ (solid curve), and an assumption for it (sum of dotted and dashed curves), at hour 14.056.

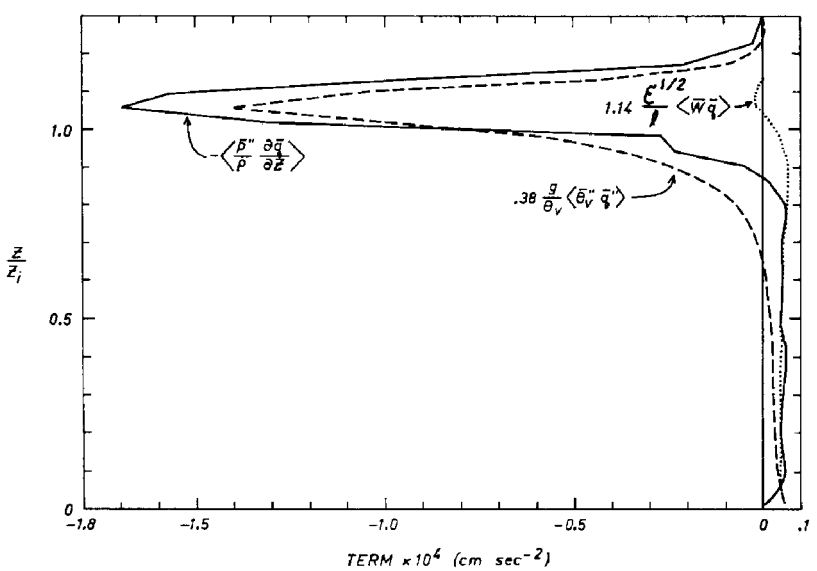

Fig. 22. Vertical profiles of $-\langle(\bar{p}''/\langle\varrho\rangle)\,\partial\bar{q}/\partial Z\rangle$ (solid curve), and an assumption for it (sum of dotted and dashed curves), at hour 14.056.

somewhat larger than 1/3 in this region, if utilized in the subgrid equations used in the computations, would have helped remove the apparently spurious subgrid moisture flux obtained in the vicinity of 1.09 z_i and discussed in connection with the production term of Figure 14.

Again it is to be hoped that coefficients such as c_S and a are more universal if applied to subgrid-scale fluctuations for a relatively small grid volume. However, it is disturbing that the grid volume used herein may not have been small enough to fulfill this hope. Even more disturbing is the ratio of about 2.6 found here for c_M/c_S whereas a ratio of unity was specified for the corresponding constants in the subgrid equations utilized in this study. Values nearly equal to unity for this ratio have been found for the surface layer by Mellor (1973) and Lewellen and Teske (1973), who used no buoyancy compensation term. It could thus be argued that for a better comparison, c_S should be evaluated from Figure 21, say, assuming $a=0$. If this is done in the interval $0.2<z/z_i<0.6$ where the shapes of the profiles of the pressure-correlation and $\langle \bar{w}\bar{\theta}_v \rangle$ terms are quite similar, and likewise for c_M in the same interval, one finds $c_M/c_S \approx$ $\approx 2.6/1.6=1.6$. This ratio is considerably closer to the expected value. However, it must be concluded that the evaluation of c_M, c_S or a for use with a model which employs large-scale or ensemble-averaged quantities will produce ambiguous values because the Rotta-type assumption is only qualitatively correct.

6. Main Conclusions

The main finding of this study is that entrainment at the top of a growing mixed layer strongly influences turbulence statistics involving specific humidity. Under conditions when the air aloft is relatively dry and the moisture flux near z_i is a large fraction of the surface flux, the profile and magnitude of the normalized humidity variance is found to be affected even in the surface layer and to be larger than the normalized temperature variance. The dissimilarity occurs because the normalized sensible heat flux, unlike the similarly scaled moisture flux, retains a nearly unique profile, decreasing smoothly with height to a small negative value at the top of the mixed layer. Only with a relatively large evaporation rate at the surface, or near-absence of a humidity gradient at the top of the mixed layer, can similarity between temperature and humidity turbulence statistics be expected in the lower part of the mixed layer. The entraining dry air is also deduced to be responsible for the differing spectral shapes for temperature and humidity. The humidity and temperature fluctuations are found to be positively correlated in the lower part of the mixed layer, but strongly negatively correlated in the upper portion.

Relative to a model mixed layer which is constrained to have no entrainment at the top of the boundary layer, an entraining mixed layer yields the following: a much larger humidity variance throughout and especially near z_i, a much larger temperature variance in the upper 20%, a horizontal velocity variance which does *not* exhibit a sharp peak at the top of the mixed layer, and a normalized vertical-velocity variance which is not much different in the two cases except near and above z_i.

The diffusion term, which represents vertical transport of the local covariance in the budget equation for the mean covariance, is found to be very important in most of the mixed layer in the budget equations for kinetic energy, temperature variance and specific-humidity variance. It is found to be much less important in the budget equations for the mean heat and moisture fluxes.

The pressure-diffusion term on a resolvable scale is found to be relatively unimportant in the turbulence kinetic energy equation. The importance of the pressure scalar-gradient correlation term is confirmed in the heat-flux and moisture-flux budget equations. If this correlation term is approximated by a Rotta-type assumption, it is found extremely important to include the expected buoyancy-compensation term near the top of the mixed layer.

The calculated spectra of vertical velocity exhibit peak energy (on a log-log plot) at a wavelength of about $2\,z_i$ in the central part of the mixed layer. These and other spectra suggest that the inertial subrange in this region commences at a wavelength of about $0.6\,z_i$.

Acknowledgement

I appreciate the helpful comments on the manuscript by Dr Larry Mahrt, Department of Atmospheric Science, Oregon State University.

References

Batchelor, G. K.: 1953, *The Theory of Homogeneous Turbulence*, University Press, Cambridge, 197 pp.

Clarke, R. H., Dyer, A. J., Brook, R. R., Reid, D. G., and Troup, A. J.: 1971, 'The Wangara Experiment: Boundary Layer Data', CSIRO Div. of Meteorol. Phys., Tech. Paper No. 19, 340 pp.

Crow, S. C.: 1968, 'Viscoelastic Properties of Fine-Grained Incompressible Turbulence', *J. Fluid Mech.* **33**, 1–20.

Deardorff, J. W.: 1972a (D1), 'Numerical Investigation of Neutral and Unstable Planetary Boundary Layers', *J. Atmospheric Sci.* **29**, 91–115.

Deardorff, J. W.: 1972b, 'On the Magnitude of the Subgrid Scale Eddy Coefficient', *J. Comp. Phys.* **7**, 120–133.

Deardorff, J. W.: 1973, 'The Use of Subgrid Transport Equations in a Three-Dimensional Model of Atmospheric Turbulence', *J. Fluids Eng.*, Sept., 429–438.

Deardorff, J. W.: 1974 (D2), 'Three-Dimensional Numerical Study of the Height and Mean Structure of a Heated Planetary Boundary Layer', *Boundary-Layer Meteorol.* **7**, 81–106.

Lenschow, D. H.: 1970, 'Airplane Measurements of Planetary Boundary Layer Structure', *J. Appl. Meteorol.* **9**, 874–884.

Lenschow, D. H.: 1974, 'Model of the Height Variation of the Turbulence Kinetic Energy Budget in the Unstable Planetary Boundary Layer', *J. Atmospheric Sci.* **31**, 465–474.

Lewellen, W. S. and Teske, M.: 1973, 'Prediction of the Monin-Obukhov Similarity Functions from an Invariant Model of Turbulence', *J. Atmospheric Sci.* **30**, 1340–1345.

Lilly, D. K.: 1967, 'The Representation of Small-Scale Turbulence in Numerical Simulation Experiments', in *Proceedings of the IBM Scientific Computing Symposium on Environmental Sciences*, White Plains, N.Y.

Lumley, J. and Khajeh-Nouri, B.: 1974, 'Computational Modeling of Turbulent Transport', in *Turbulent Diffusion in Environmental Pollution*, (*Adv. Geophys.* **18**), F. N. Frenkiel and R. E. Munn, (eds.), Academic Press, Inc., New York.

Mellor, G. L.: 1973, 'Analytic Prediction of the Properties of Stratified Planetary Boundary Layers', *J. Atmospheric Sci.* **30**, 1061–1069.

Phelps, G. T. and Pond, S.: 1971, 'Spectra of the Temperature and Humidity Fluctuations and of the

Fluxes of Moisture and Sensible Heat in the Marine Boundary Layer', *J. Atmospheric Sci.* **28**, 918–928.

Rotta, J.: 1951, 'Statistische Theorie Nichthomogener Turbulenz', *Z. Phys.* **129**, 547–572.

Telford, J. W. and Warner, J.: 1964, 'Fluxes of Heat and Vapor in the Lower Atmosphere derived from Aircraft Observations', *J. Atmospheric Sci.* **21**, 539–548.

Willis, G. and Deardorff, J. W.: 1974, 'A Laboratory Model of the Unstable Planetary Boundary Layer', to appear in *J. Atmospheric Sci.* **31**.

Wyngaard, J. C.: 1973, 'On Surface-Layer Turbulence', in *Workshop in Micrometeorology*, D. A. Haugen (ed.), American Meteorological Society, Boston, Mass., pp. 101–149.

Wyngaard, J. C. and Coté, O. R.: 1971, 'The Budgets of Turbulent Kinetic Energy and Temperature Variance in the Atmospheric Surface Layer', *J. Atmospheric Sci.* **28**, 190–201.

Wyngaard, J. C., Coté, O. R., and Izumi, Y.: 1971, 'Local Free Convection, Similarity, and the Budgets of Shear Stress and Heat Flux', *J. Atmospheric Sci.* **28**, 1171–1182.